Dynamics of passive tracers in the atmosphere: Laboratory experiments and numerical tests with reanalysis wind fields

Imre M. Jánosi,[1,2] Péter Kiss,[1] Viktória Homonnai,[2] Margit Pattantyús-Ábrahám,[2] Balázs Gyüre,[2] and Tamás Tél[2,3]

[1]*Department of Physics of Complex Systems, Eötvös Loránd University, Pázmány P. s. 1/A, H-1117 Budapest, Hungary*

[2]*von Kármán Laboratory of Environmental Flows, Eötvös Loránd University, Pázmány P. s. 1/A, H-1117 Budapest, Hungary*

[3]*Department of Theoretical Physics, Eötvös Loránd University, Pázmány P. s. 1/A, H-1117 Budapest, Hungary*

Laboratory and numerical experiments are reported on dye advection processes in geostrophic turbulence. The experimental setup is the classical rotating annulus with differential heating which mimics the most essential features of midlatitude atmospheric flow. The main control parameter is the temperature contrast. Fluorescent dye is used as passive tracer, and dispersion is evaluated by digital image processing. The results are compared with tracer dispersion computations which are performed by means of global reanalysis wind fields at the pressure height of 500 hPa covering a time interval of one year. Apart from initial transient periods, the characteristic behavior for intermediate time scales is *ballistic* dispersion in both systems, where the zonal extent of the tracer cloud increases *linearly* in time (Batchelor scaling). The long-time evolution cannot be followed by the experimental technique, however, the numerical tests suggest a slower *diffusive* dispersion (Taylor regime) after 70–80 revolutions (days), in agreement with expectations. Richardson-Obukhov scaling (superdiffusion with an exponent value of 3/2) is neither observed in the laboratory nor in the numerical tests. Our findings confirm recent experimental results on the classic prediction by Batchelor that the initial pair separation is an essential parameter of the subsequent time evolution of tracers.

PACS number(s): 47.27.T−, 92.60.hk

I. INTRODUCTION

Anthropogenic emissions often lead to pollution levels that exceed air quality standards at many locations over both hemispheres [1–3]. Air quality and pollutant deposition are also influenced by transport processes at the intercontinental and global scales. The most spectacular pollution transport events are related to export from the east coasts of North America or Asia with subsequent transport to the west coasts of Europe and North America.

As a topical example, the recent eruption of the subglacial volcano Eyjafjallajökull in Iceland threw volcanic ash several kilometers up in the atmosphere which led to air traffic disruption in northwest Europe for several days in April and in May 2010, including the closure of airspace over many parts of Europe (Fig. 1).

Tracer transport and mixing processes are also relevant in the aqueous environment [5–7]. On the largest scales, the same governing equations of motion can be used both in the atmosphere and oceans, therefore the tools to study tracer advection are also very similar. Empirical data mostly originate from drifter experiments, such as the Global Drifter Program (http://www.aoml.noaa.gov/phod/dac/gdp.html) or the recent POLEWARD project [8]. Atmospheric measurements are running from the seventies, the first large balloon experiments were performed over the southern hemisphere: the EOLE at 200 mb [9,10], and the TWERLE at 150 mb pressure level [11,12]. Besides numerical simulations [13,14], laboratory models [15] provide a deeper insight into the physical basis of the key processes.

Here we compare the results of laboratory and numerical experiments on tracer dispersion. The key quantities of interest are the mean drift of the "center of mass," and the spread of the cloud related to the average pair separation. The lit-erature concerning pair dispersion both in two-dimensional (2D) and three-dimensional (3D) turbulent flows is quite controversial, in spite of the intense research in the past decades (see Refs. [16,17] and references therein). The main problem is that the dynamics suffers from a series of cross-over behavior from exponential to power-law dispersion with various exponent values, and the crossover points cannot be easily located since they depend on several factors. A recent challenging experimental result is that the time evolution strongly depends on the initial pair separation [17], thus in usual laboratory or numerical experiments the dynamics re-

Total column of VO-TR and 500 hPa geopotential
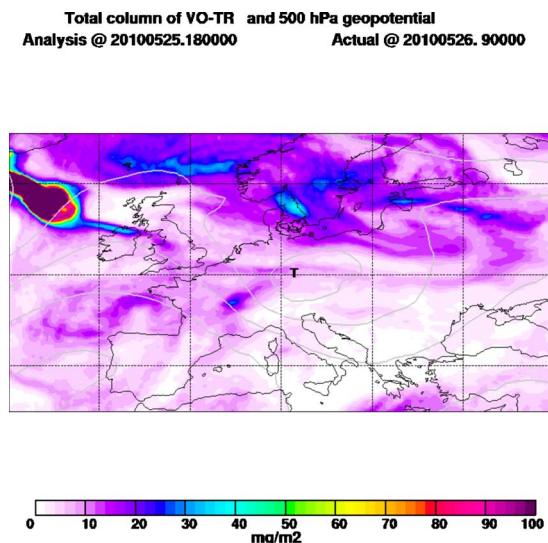Analysis @ 20100525.180000   Actual @ 20100526. 90000

FIG. 1. (Color online) Example snapshot of emitted volcanic ash distribution forecast for the Eyjafjallajökull eruption, 05/25/2010, by the FLEXPART model [4]. (http://transport.nilu.no/)
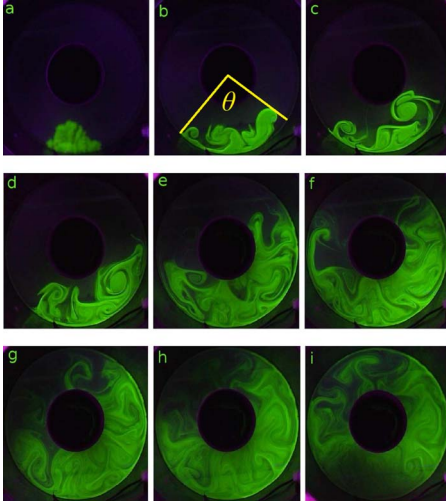
FIG. 2. (Color online) The spread of fluorescent dye as a function of time at parameters $\Delta T = 31.5$ °C, $\Omega = 1.62$ rad/s, $H = 3.4$ cm ($\mathrm{Ro}_T = 0.0209$). (a) 1 s, (b) 8 s, (c) 19 s, (d) 46 s, (e) 120 s, (f) 154 s, (g) 197 s, (h) 235 s, (i) 244 s. The angle θ characterizes the zonal range covered by the cloud.

flects a mixed behavior when the evaluation of individual trajectories is not possible.

Our experiments were carried out in the classical laboratory model for midlatitude large-scale flow phenomena, which is a differentially heated rotating annulus invented by Fultz [18,19] and Hide [20,21]. Fluorescent dye forms a localized cloud of passive tracers after geostrophic turbulence has established, subsequent time evolution can be evaluated by digital image processing (Fig. 2). The numerical experiments are based on the equations of passive scalar advection, where the background wind field is provided by the ERA-Interim data bank of the European Centre for Medium-Range Weather Forecasts (http://www.ecmwf.int/research/era/). Both systems exhibit very similar behavior. The initial transients (short time dispersal) cannot be evaluated because of the macroscopic perturbation induced by dye injection in the experiments, and because of the limited spatial and temporal resolution of the reanalysis wind field in the numerical tests. The dispersal is "ballistic" for intermediate time intervals characterized by a linear growth of the zonal extent of the tracer cloud. This dynamics is not expected from theoretical considerations [16], but it is identified in other numerical [22,23] and experimental works [17]. When strong correlations produced by coherent structures in the flow decay at longer times, a switch to diffusive dispersal is expected. We could identify this regime only in the numerical simulations.

The paper is organized as follows. Section II provides a description of the physical background, laboratory experiments, and evaluation techniques. The results are listed in Section III. Section IV gives an overview of the numerical simulations of tracer dispersion driven by ECMWF reanalysis wind field for the year of 2000. The two sets of results are compared and contrasted with theoretical predictions in Sec. V closed by a compact summary.

II. EXPERIMENTS

The setup, also described in [24], consists of three concentric cylinders of radii $R_1 = 4.5$, $R_2 = 15.0$, and $R_3 = 20.3$ cm which is fixed on a rotating platform. The central container is filled up with a mixture of ice and water, the outermost one is regulated by an immersion heater, the working fluid in the middle annular region is tap water in the presented experiments. The main control parameters are the angular velocity $\Omega \in [1.54, 2.31]$ rad/s and imposed radial temperature difference $\Delta T \in [15.0, 40.5]$ °C in the dish. The height H of the working fluid is varied in a narrow range of 3.3–4.0 cm in order to warrant that the dynamics is well inside the geostrophic turbulent regime [25,26]. The convenient nondimensional combination known as thermal Rossby number (Ro_T) is defined as

$$\mathrm{Ro}_T = \frac{\alpha g H \Delta T}{(2\Omega)^2 L^2}, \tag{1}$$

where $\alpha \approx 2 \times 10^{-4}$ °C^{-1} is the coefficient of volumetric thermal expansion for water, $g = 9.81$ ms^{-2}, and $L = R_2 - R_1 = 0.105$ m.

The thermal Rossby number has a fairly transparent explanation by considering a possible stationary situation, the geostrophic equilibrium, where pressure gradient and Coriolis forces balance each other [27]. In that case, the zonal velocity component u_θ in a corotating frame of reference is determined by the radial pressure difference as

$$u_\theta = -\frac{1}{\rho_0 2\Omega} \frac{\partial p}{\partial r}, \tag{2}$$

where ρ_0 is a mean density of the fluid at a reference temperature T_0, and friction is neglected. The pressure difference is a consequence of radial temperature contrast inducing a change in density $\Delta\rho = -\alpha\rho_0\Delta T$. Using the hydrostatic approximation $p = \rho g H$, the radial pressure difference in a shallow layer can be estimated as $\Delta p = -\alpha\rho_0 g H\Delta T$, which gives an estimate to a relative velocity scale

$$U = \frac{\alpha g H \Delta T}{2\Omega L}. \tag{3}$$

A simple comparison with Eq. (1) reveals that the thermal Rossby number is in full analogy with the "regular" one, since it is given as the ratio of two characteristic velocity scales,

$$\mathrm{Ro}_T = \frac{U}{2\Omega L}. \tag{4}$$

The parameter range $\mathrm{Ro}_T \in [0.01, 0.1]$ we implemented is deeply in the dynamical regime of irregular wave patterns, similarly to the midlatitude atmosphere. This similarity is apparent in Fig. 2, where snapshots of a typical experiment are displayed: after an appropriate spinup period, 1 ml of standard fluorescent dye (Sodium fluorescein, $C_{20}H_{10}O_5Na_2$) is injected through a syringe at a location close to the second cylinder wall of radius R_2, and the development of patterns is recorded and evaluated by digital image processing. The dominating patterns clearly indicate strong irregular cyclonic
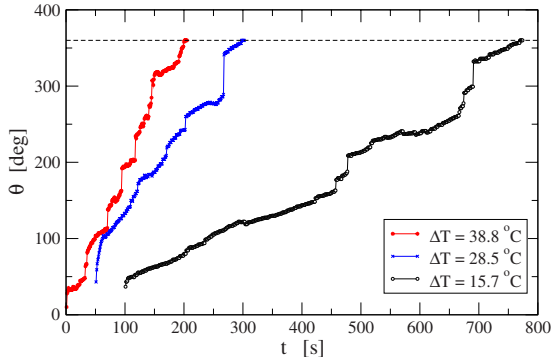
FIG. 3. (Color online) Time evolution of θ (see Fig. 2) at three different temperature contrasts (see legend). The other parameters were almost identical, the precise values are $Ro_T=0.0272$, 0.0209, and 0.0110, corresponding to curves from left to right.

and anticyclonic vortical activity. It is widely accepted that this dynamics driven by the so called baroclinic instability reflects the most essential features of midlatitude atmospheric flow (see, e.g., [28,29]).

Two quantities are determined to characterize dye dispersion. The first one is the maximal zonal extent of the dye cloud measured by the central angle θ bounding the colored region [see Fig. 2(b)]. Second, the total number of pixels n above a contrast threshold is also determined at each frame. In order to decrease the effects of nonuniformities in UV illumination (see Fig. 2), an averaging over one revolution is performed prior to further processing.

Figure 3 illustrates typical time evolution of the bounding angle $\theta(t)$ for three different temperature contrasts. As expected, stronger convective drives result in larger slopes (faster zonal growth). The intermittent nature of the dispersion is also clear, slow increments are sometimes followed by sudden jumps, when a new empty vortex grabs a filament of dye. The curves for the total pixel number (or cloud area) $n(t)$ are very similar (see later), however their intermittent character is much weaker.

III. EXPERIMENTAL RESULTS

Besides the intermittency, the overall tendency of $\theta(t)$ curves seems to be linear (Fig. 3). Since theories predict diverse behavior from exponential to power-law dispersion with various exponent values, we evaluated the data by testing all possibilities.

Figure 4 illustrates one example on a double-logarithmic scale (see symbols, the rightmost curve in Fig. 3). It is certainly not a pure power law, therefore we show its numerical integral as well (upper curve, Fig. 4) in order to test the well-known noise suppression property of integration. Several attempts to achieve the best power-law fits have led to the conclusion that the overall time evolution is close to linear, therefore we use this assumption in what follows.

To determine characteristic slopes for the $\theta(t)$ curves, both the usual linear form $\theta(t)=m_\theta t+\theta_0$ and its integral $\int \theta(t)dt=0.5m_\theta t^2+\theta_0 t+c$ are fitted. Figure 5 demonstrates a reasonable data collapse after rescaling $\theta(t)$ values by the
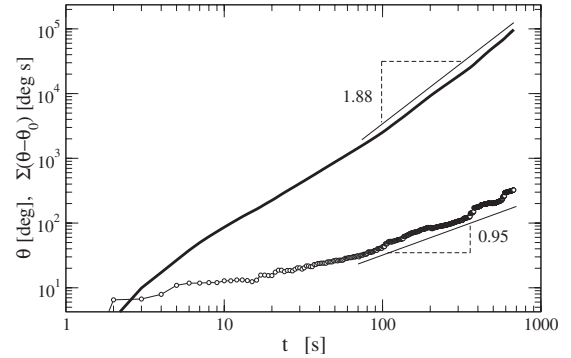

FIG. 4. The rightmost measured curve of Fig. 3 (symbols) and its numerical integral (upper curve) on a double-logarithmic scale. Asymptotic power-law fits are indicated. Parameters: $\Delta T=15.75 \pm 0.25$ °C, $\Omega=1.56$ rad/s, $H=3.3$ cm ($Ro_T=0.0110$).

individual fitted slopes m_θ and intercepts θ_0. Deviations from pure linear time evolution are clear for any of the specific records, especially for larger times, however, we did not find a convincingly better approximation for the general behavior than a linear growth.

Figure 6 exhibits the dependence of fitted slopes m_θ on the experimental control parameter, the thermal Rossby number Ro_T of Eq. (1). Note that vertical bars indicate the standard error of the coefficient given by the fitting algorithm. Certainly more important error sources such as deficiencies in the temperature control, significant initial perturbations at dye injection or thresholding errors in the identification of dye cloud edges contribute to the scatter of data points, however, we cannot give a quantitative estimate of these effects. The apparent uncertainties are especially large for large values of Ro_T, where the slopes m_θ cannot be determined by direct fitting, because the records are too short and very intermittent. Instead, an estimate is given based on the encompassing time t^* defined as $\theta(t^*)=360°$ (red squares in Fig. 6). Figure 6 suggests a simple linear dependence $m_\theta \sim Ro_T^\gamma$ with $\gamma \approx 1$.

The large apparent uncertainties in the slopes m_θ (Fig. 6) motivated a consistency check based on the encompassing time t^* defined above. Values for t^* were extracted and expressed as a dimensionless number $N=t^*\Omega/2\pi$, which is the
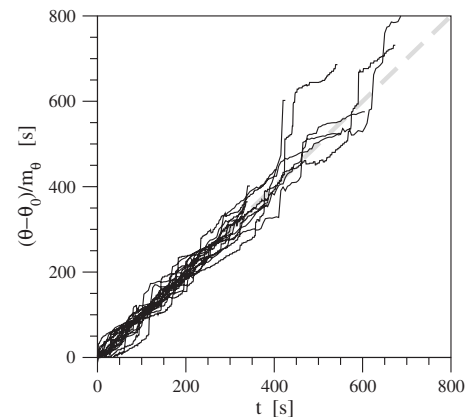

FIG. 5. Data collapse using the linear (ballistic) dispersion assumption for 24 measured data sets: $\theta(t)=m_\theta t+\theta_0$.
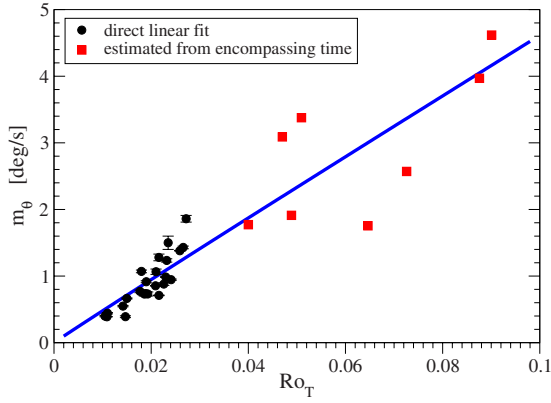
FIG. 6. (Color online) Slope of linear fits m_θ as a function of thermal Rossby number Ro_T (circles). The slopes for fast dispersion processes (red squares) were estimated from the encompassing time (see text). Heavy line illustrates a power-law fit with an exponent of $\gamma = 0.98 \pm 0.07$.

number of revolutions until the leading and tailing edges of the cloud cross the same "longitude" in the rotating annulus. In order to minimize the effect of different initial configurations, the measured temporal interval of $t(\theta_0 \rightarrow 360°)$ is extrapolated to $t(0 \rightarrow 360°)$ assuming the same average zonal spreading velocity. The result is plotted in Fig. 7. Note that N is determined independently of the fitting procedure to obtain m_θ for the 24 experiments indicated by black circles in Fig. 6, it is calculated directly from the recorded data point at $\theta = 360°$. The relationship is clearly an inverse function $N \sim Ro_T^{-1}$ which is consistent with Fig. 6: the stronger the convective drive the lower the number of revolution until a "hemispheric" encompassing.

As for the second measure, the total size of the dye cloud $n(t)$ determined in units of pixels exhibits a linear growth as well. Figure 8 shows data collapse of rescaled curves by two characteristic crossover parameters $t_\times$ and $n_\times$. The general time evolution is clearly linear, which proceeds to a given time $t_\times$, where a crossover to a constant apparent cloud size
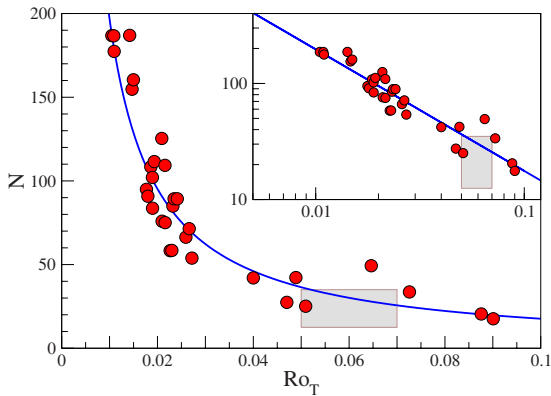

FIG. 7. (Color online) Number of revolutions N until the zonal spread of the dye cloud covers a whole circle as a function of thermal Rossby number Ro_T. The inset shows the same data on a double-logarithmic scale. The continuous line is an inverse relationship $N \sim Ro_T^{-1}$. Shaded rectangle indicates plausible range for the rotating Earth (see Sec. IV).
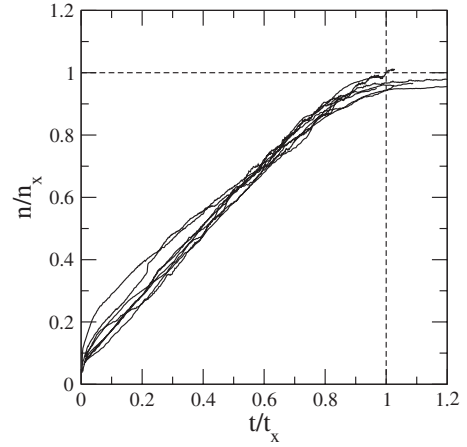

FIG. 8. Scaled total area $n/n_\times$ covered by the fluorescent dye as a function of scaled time $t/t_\times$ for eight representative experiments. The scaling parameters $n_\times$ (in units of pixel) and $t_\times$ (in units of s) belong to the crossover values where the apparently linear curves saturate.

$n_\times$ is visible (Fig. 8). According to our observations, this plateau $n_\times$ (in units of pixels) is not necessarily constant for each experimental run. This is because the dispersion process has at least three competing ingredients with different weights at a particular set of parameters: the most spectacular changes are due to (chaotic) advection by the background flow field, meanwhile local shearing contributes to mixing mostly between vortex walls and cores (sometimes with nice Kelvin-Helmholtz billows), and additionally diffusional thinning continuously decreases the fluorescent intensity. The general tendency is that the larger $t_\times$ the lower $n_\times$. We think that a further quantitative analysis is not necessary here because the numerical values for saturation parameters $n_\times$ and $t_\times$ are fully specific for our setup (camera sensitivity and resolution, geometric parameters, etc.). Instead, we plot the slopes m_n of linear growth $n(t) = m_n t + n_0$, as a function of Ro_T in Fig. 9. A simple power-law behavior stands out again, with an approximately quadratic behavior as a function of the control parameter: $m_n \sim Ro_T^\delta$ with $\delta \approx 2$. (The number of data points is different in Figs. 6 and 9, because experiments
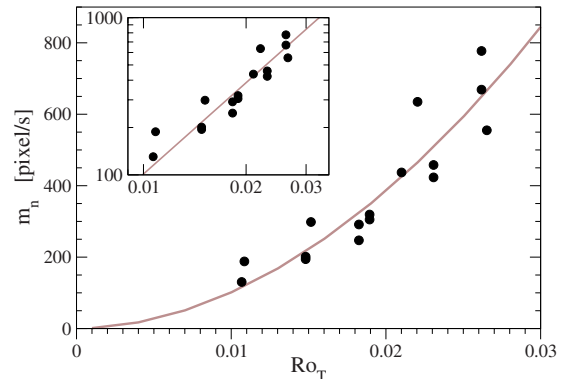

FIG. 9. (Color online) Slope of linear fits m_n as a function of thermal Rossby number Ro_T. The inset shows the same data on a double-logarithmic scale. Heavy lines illustrate power-law fit with an exponent of $\delta = 1.93 \pm 0.18$.

with $\mathrm{Ro}_T > 0.03$ resulted in short and noisy records, thus they are omitted.)

Note that in the existing literature we could not find any theoretical prediction for a relationship between the exponent values γ and δ. As we explained above, the dispersion of a tracer cloud exhibits complex dynamics with various subprocesses resulting in fractal structures (see Fig. 2), therefore we do not expect that a linear measure (e.g., the zonal extent θ) has necessarily a trivial relationship with a composite measure (e.g., total cloud size n).

IV. NUMERICAL SIMULATIONS

In order to check the performance of laboratory experiments in reproducing some basic aspects of midlatitude atmospheric transport processes, a plausible method is to compare the results with numerical experiments on tracer advection [5]. Various methods to compute trajectories have been developed, and the accuracy of calculated trajectories has improved a lot in the past decades [30,31]. Theoretically, atmospheric trajectories can be calculated directly from wind observations by interpolating between the measuring locations. In practice, however, trajectory calculations are mostly based on gridded output of numerical models (weather forecasts or reanalyses) such as provided by the European Centre for Medium-Range Weather Forecasts (ECMWF) [32].

In this work, the 3rd generation ECMWF reanalysis ERA-Interim data bank is exploited, which is almost up to date from 01/01/1989 [33]. Zonal (u) and meridional (v) wind velocity components of global geographic coverage at the pressure level of 500 hPa (an approximate altitude of 5–5.5 km) are evaluated for the whole year of 2000. Four values are available each day for 00, 06, 12, and 18 h UTC (Universal Time Coordinated) at each geographic location with a spatial resolution of $1.5° \times 1.5°$ (lat/long). Note that the gridded wind fields are rather smooth, subgrid scale turbulence or vertical convection are not resolved. Although the wind velocity at a given site and time represents an instantaneous value [32], direct comparison with high resolution wind tower measurements indicates that it is better to regard it as a 6 h mean value [34].

Trajectory calculation are based on the solution of the advection equation for a given infinitesimal air parcel [35,36],

$$\frac{d\mathbf{r}}{dt} = \mathbf{v}[\mathbf{r}(t)], \tag{5}$$

where $\mathbf{v}[\mathbf{r}(t)]$ is the instantaneous velocity at the position $\mathbf{r}(t)$. Equation (5) can be solved analytically for simple flow fields only, more realistic situations require a numerical treatment based on the finite difference Taylor-series representation [31].

Our primary goal is to give a statistical characterization of atmospheric dispersal instead of calculating accurate trajectories, therefore we use the simplest approximations wherever possible. The temporal and spatial resolutions of ERA-Interim wind fields purport the most significant limitation, therefore very accurate atmospheric trajectories cannot be expected even by the most advanced numerical methods.
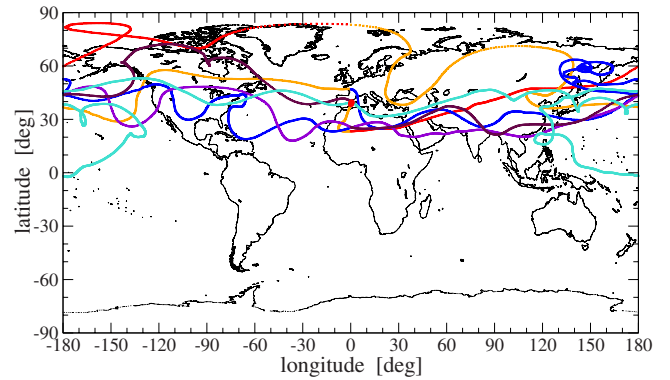

FIG. 10. (Color online) Example trajectory of a point tracer advected over the Northern hemisphere. The starting location was $45°$N, $0°$ (lat, long), different colors (greyness levels) indicate consecutive circumnavigations.

In contrast to the horizontal wind velocity vector (u, v), there are no routine observations for the vertical component w. Estimates can be produced by various meteorological models, but they are definitely less accurate than the fields of the horizontal wind. A plausible idea is to compute the 2D divergence field and estimate w from the results, however it is known that this has a very large error at the limited resolution of the reanalyses [37]. In the absence of reliable 3D wind fields, the usual procedure is to follow isobaric (constant pressure), or isentropic (constant potential temperature) surfaces with matching 2D wind velocity vectors [38]. The latter has the advantage that atmospheric variables tend to be better correlated along isentropic surfaces than on constant pressure surfaces, however, the potential temperature (entropy) of a given air parcel can significantly change when diabatic processes have an important role along a trajectory (e.g., in baroclinic stratification, which is common in midlatitude tropospheric flows) [30,31]. For this reason we evaluated the 2D wind field at the 500 hPa pressure level.

The limited spatial and temporal resolutions require the implementation of some interpolation procedures for the wind field at the numerical solution of Eq. (5). Several methods are known and tested in the literature [13,14,39]. For the time variable t, the simple linear interpolation provides a sufficiently accurate solution [39]. Computationally more demanding algorithms are used for the spatial interpolation, such as the inverse quadratic ($1/r^2$ weighting) or cubic spline approximations [40]. As for the numerical integration, the simple Euler method is implemented [40]. Consistency is checked with various time-steps of 6, 15, and 30 min (see below).

Calculated trajectory of a point tracer released from the middle of the northern hemisphere is illustrated in Fig. 10. Colors (grayness levels) change when the "particle" repeatedly crosses the initial longitude ($0°$). A couple of closed loops are easy to identify, however the general tendency is a steady drift from west to east (due to the Westerlies) along a wriggled trajectory.

Meridional transport is strongly hindered across the equator: 202 days are not sufficient for a uniform tracer distribution, as it is apparent in Fig. 11.

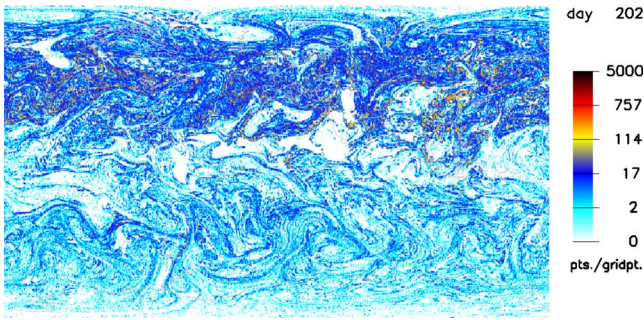The quantitative evaluation of numerical computations is much simpler than in dye dispersal experiments. The trivial

FIG. 11. (Color online) Dispersion of 10^5 point tracers started from a square of $1° \times 1°$ from the position $45°$N, $0°$ (lat, long). The snapshot is taken after 202 days of advection, the color bar (grayness level) indicates tracer density (number of particles per grid cell).

reason is that individual trajectories can be easily followed. For example, the mean center-of-mass drift velocity has an almost constant eastward zonal component of $11°/$day (~870 km/day at $45°$N) with a practically zero mean meridional component. This result is obtained from ensemble averaging over 96 numerical experiments, where clusters of 130 particles distributed on a regular lattice inside of an initial cell of $10° \times 10°$ are studied. The role of regular spacing was to avoid small tracer distances, we will return to this point in Sec. V. The center of 12 different clusters were located at equal longitudinal spacing of $30°$ along the latitudinal circle $45°$N, and each initial configuration was simulated from eight different initial time instants for 500 h long. We note that the tendency in the experimental tank is very similar to the numerical results. The snapshots in Fig. 2 are recorded by a corotating camera at positive rotation, and it is absolutely clear that the cloud dispersal is asymmetric: the right hand ("eastern") side spreads faster than the left hand ("western") edge resulting in an eastward drift of the center of mass.

The edges of the tracer clouds move with different speeds than the center of mass. The zonal spread $\theta(t)$ of the cloud is defined again as the difference between the leading and tailing edges (in angular units), in analogy with the laboratory experiments (see Fig. 2). The average behavior is illustrated in Fig. 12: the zonal spreading quickly converges to a ballistic behavior of linear growth.

The covered area fraction $A(t)$ is determined by the number of cells of $0.5° \times 0.5°$ where at least a single particle is located, normalized by the total cell number of the global mesh. Similarly to the laboratory experiments, ballistic (linear) growth appears on an intermediate time interval of 15–40 days, see the inset in Fig. 13. The long-time growth after 3–4 encompassing time periods (~60 days, c.f. Figs. 12 and 13) is close to be diffusive, as it is expected. Note, however, that the analogy with the experimental situation is limited, because the number of tracers is strictly conserved in the numerical tests, but this does not hold for the fluorescent dye as a consequence of diffusive thinning.

In Fig. 7, the experimental number or revolutions N is shown until the leading and tailing edges of the dye cloud cross the same "longitude." To improve statistics in the numerical tests, the circumnavigation (or zonal return) time t_c
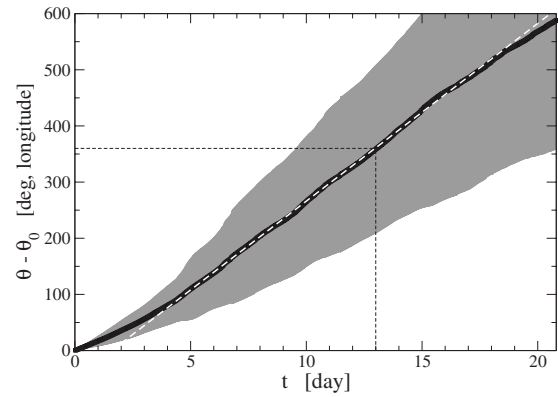

FIG. 12. Average longitudinal spread θ (see Fig. 2) of tracer clusters formed by 130 particles as a function of time (black line). Gray band indicates one standard deviation obtained from 96 numerical experiments (see text). Black dashed line marks the average encompassing time t^*, white dashed line is a linear fit.

for each individual tracer particle is evaluated. The initial configuration was a thin cloud of uniformly distributed tracers at $0°$ (longitude) over the latitude range of $80°$S–$80°$N. The circumnavigation time t_c has a very broad distribution, as illustrated in Fig. 14. Note that the encompassing time t^* of a dye cloud is related to the *width* of the distribution of single-particle circumnavigation time t_c. Broadly speaking, this width is related to the difference between the fastest and slowest tracers in a given cloud. Note also the consistency of the normalized histograms obtained at different time steps of the numerical integration. The right hand side of the empirical histograms obeys an almost cubic power-law decay. Due to the heavy tail, the mean value $\bar{t}_c \approx 23.5$ days is larger than the mode (the location of most probable value) $\hat{t}_c \approx 18.7$ days. If we intend to compare these values with the laboratory experiments, we need an estimate for the thermal Rossby number Ro_T in case of the rotating Earth. This is not a trivial task because of the differential rotation (the Coriolis
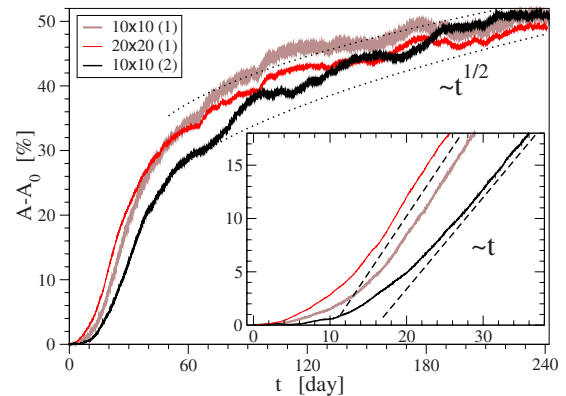

FIG. 13. (Color online) Covered area fraction $A - A_0$ as a function of time for 5×10^5 tracer particles released from clusters of two sizes (see legend) centered at $45°$N, $0°$ in case (1), top two curves, and $45°$N, $30°$E in case (2), bottom curve. Area computations are performed by a resolution of $0.5° \times 0.5°$. Dotted lines indicate diffusive growth with $t^{1/2}$ behavior. Inset: zoom to the initial part. The growth is linear for intermediate times (dashed lines).
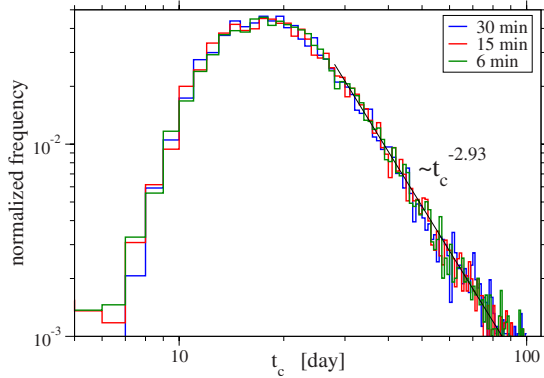
FIG. 14. (Color online) Empirical probability density distribution of the circumnavigation time t_c for three numerical experiments with 10^3 tracers and temporal resolutions of 6, 15, and 30 min. The initial condition was a uniform spatial distribution along the longitude 0° in the range of [80°S, 80°N] latitude. The decay obeys an approximately cubic power-law for large t_c values (note the double-logarithmic scale).

parameter changes with the latitude) and the different thermal boundary conditions. Still, when we assume that the laboratory setup adequately models midlatitude atmosphere between 30°–70° [24], an approximate mean temperature difference can be $\Delta T \approx 25 - 30$ °C. Relevant length scales are $H = 10$ km, $L = 4500$ km, a mean Coriolis parameter [replacing 2Ω in Eq. (1)] is $f \approx 10^{-4}$ s^{-1}, and an average coefficient of volumetric expansion for air is $\alpha \approx 4 \times 10^{-3}$ °C^{-1}. An estimated thermal Rossby number [see Eq. (1)] should fall in the range [0.05–0.07]. By comparing Figs. 7 and 14, we can see that numerical results are consistent with the laboratory experiments and thus with the underlying assumptions.

The last presented numerical result in Fig. 15 cannot be compared with the laboratory experiments. It illustrates an interesting focusing effect in the atmosphere that is tracers started from a uniform meridional distribution have a tendency to drift toward the middle latitudes on both hemispheres during the advection. The results of four experiments
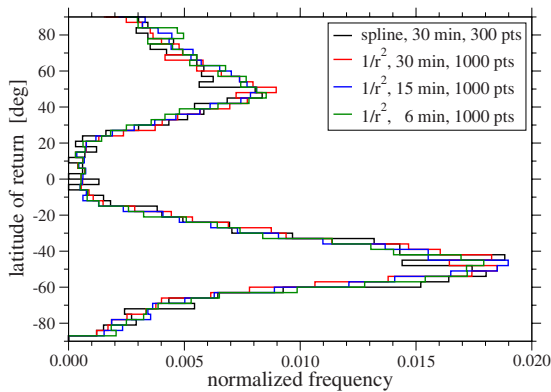

FIG. 15. (Color online) Asymptotic empirical probability density distribution of the latitude of return on an inverted scale. Four different numerical experiments are performed with different spatial interpolation schemes, integration time-steps, and cluster sizes (see legend). The initial condition was a uniform meridional distribution along the longitude 0° in the range of [80°S, 80°N] latitude.

with different integration step sizes and spatial interpolation methods (inverse quadratic and cubic spline) are plotted together to demonstrate again statistical consistency. The asymptotic distribution is obtained after 1 year of advection, where the last latitude value at crossing 0° longitude is recorded. A similar focusing effect was reported in Ref. [41] by simulating trajectories over isentropic surfaces, however they studied tracer density distributions at fixed time differences.

V. DISCUSSION

The motion of an incompressible turbulent fluid is described by the Navier-Stokes equation amended by the incompressibility condition of zero divergence. According to Kolmogorov's (K41) similarity theory [42], the largest spatial and temporal scales are given by the energy-injection length scales $\mathcal{L}$ and eddy turnover time $T_{\mathcal{L}}$, while the smallest scales are given by the Kolmogorov length $\eta = (\nu^3/\epsilon)^{1/4}$ and the Kolmogorov time $\tau = \sqrt{\nu/\epsilon}$ (where ν is the kinematic viscosity, and ϵ is the energy dissipation rate per unit mass). The interval $(\eta, \mathcal{L})$ is known as the inertial subrange because viscous dissipation becomes important only at scales $l < \eta$.

Theoretical description of the mean square separation between two fluid elements $\langle r(t)^2 \rangle$ in the inertial subrange is dated back to 1926, when Richardson suggested that it should grow in time as t^3 [17,43]. Obukhov specified that in homogeneous and isotropic 3d turbulence, the pair dispersion should grow as $\langle r(t)^2 \rangle = g \epsilon t^3$, where g is a universal constant. Batchelor refined this work [44] by considering the role of initial separation $r_0 \equiv r(t=0)$, and concluded that the mean square separation should grow as t^2 for times shorter than a characteristic time scale $t_0 = (r_0^2/\epsilon)^{1/3}$,

$$[\langle r(t)^2 \rangle - r_0^2] = \frac{11}{3} C_2 (\epsilon r_0)^{2/3} t^2, \tag{6}$$

where $C_2 \approx 2.13$ is the scaling constant for the second-order Eulerian velocity structure function [17], and $t \ll t_0$. In the classical K41 theory of turbulence, t_0 may be identified as the time for which the divergence of two fluid elements is determined by their initial relative velocity $\Delta \mathbf{v}_0$ in a given eddy of size r_0. At times $t > t_0$, the growth of the pair separation is expected to follow the Richardson-Obukhov scaling, independently of r_0. When the separation exceeds the size of largest coherent structures, diffusive dispersion is expected $\langle r(t)^2 \rangle \sim t$ (Taylor regime). In statistically stationary forced homogeneous and isotropic two-dimensional turbulence, the Richardson-Obukhov t^3 scaling holds, however experiments exhibited various empirical exponent values between 2 and 3 [16,45].

An essential condition behind the validity of the Batchelor scaling Eq. (6) is the lack of correlations between the initial separation $\mathbf{r}_0$ and the relative velocity of the pair $\Delta \mathbf{v}_0$ [43]. When this condition is not fulfilled, the correct scaling form of relative pair separation is based on the vectorial difference as

$$\langle |\mathbf{r}(t) - \mathbf{r}_0|^2 \rangle = \frac{11}{3} C_2 (\epsilon r_0)^{2/3} t^2. \tag{7}$$
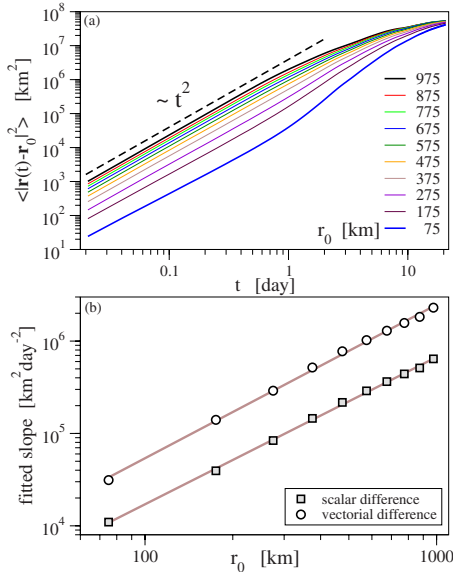
FIG. 16. (Color online) (a) Mean squared relative pair separation for 96 dispersal experiments (see text) determined by the vectorial difference [see Eq. (7)], and binned for different initial separations (see legend, curves from top to bottom). The dashed line illustrate t^2 scaling. (b) Fitted slopes as a function of initial separation r_0 by using the scalar/vectorial definition Eqs. (6) and (7), see legend. The fitted exponent values are 1.66 ± 0.02 (white circles) and 1.59 ± 0.03 (filled squares).

Note that this Batchelor form bears important consequences related to the evaluation of experimental data. (i) When the energy dissipation rate per unit mass ϵ is fixed, the rate of pair separation depends on the initial value r_0 itself. (ii) The transition time to Richardson-Obukhov scaling t_0 depends also on r_0. This means that one cannot observe a "clean" dynamics in a cloud of tracers with a mixture of various initial separations. (iii) Identification of Richardson-Obukhov t^3 scaling requires also a significant time scale separation between t_0 and the eddy turnover time $T_{\mathcal{L}}$ [8,43]. Since the latter quantity is estimated around 3–5 days in the troposphere (considering scales of a typical midlatitude cyclone) [46], and values for ϵ are around 10^{-5} m^2/s^3 [47], an initial pair separation of $r_0 \approx 300-500$ km easily produces t_0 on the order of a day.

A direct check of Batchelor hypotheses is possible only by means of numerical simulations, because Lagrangian pair tracking is not feasible by our experimental techniques. Here we show representative results for the 96 dispersal simulations, where the average pair separation is determined by both scalar and vectorial definitions Eqs. (6) and (7). Individual clusters (12 locations and 8 starting time instants, as before) are formed by 130 regularly spaced tracers over a geographic area of $10° \times 10°$. The time dependence of pair separation was determined in initial distance bins of 50 km, where the center values are indicated in the legend of Fig. 16(a) (thus bin "75 km" denotes 50 km$< r_0 <$100 km, etc., except the largest value where "975 km" means r_0 >950 km).

A special feature emerges at the vectorial differences in Eq. (7) because pair dispersion proceeds over a spherical

surface. The definition for $[\mathbf{r}(t) - \mathbf{r}_0]$ is unambiguous in 3D Euclidean sense, however, pair distances must be determined along geodesics in the atmosphere at large enough separations. To avoid computational discrepancies, we adopted the following convention. One of the points of each pair is favored throughout the computations, and the angles are calculated in the comoving Euclidean frame of reference (zonal x and meridional y axes) with origin at this point. Vector lengths are calculated on geodesics. This procedure is not unique, however, we checked that the statistics conforms with Eq. (6) where scalar separations were computed by pure spherical geometry.

The results in Fig. 16(a) are consistent with the Batchelor hypothesis over almost two decades of the time axis: the mean squared separation increases with t^2, and the slopes depend on the initial value r_0. We emphasize that the behavior is almost the same for both the scalar and vector distances [Eqs. (6) and (7)], apart from numerical values for the slopes shown in Fig. 16(b). Here, the empirical scaling is somewhat surprising, because the exponent value $\sim 5/3$ is very far from $2/3$ [see Eqs. (6) and (7)], it cannot be a simple consequence of numerical inaccuracies or statistical errors. We are fully aware of the fact that large scale dispersal in the atmosphere (and in the laboratory tank) can be different from what one expects in 3D homogeneous and isotropic turbulence, still the theoretical predictions concerning the time dependence are very similar in both systems.

Let us summarize our findings in a compact form:

(i) We have shown that the zonal spread of a passive tracer cloud grows *linearly* in time both in the rotating tank experiments (Fig. 5) and in the numerical advection simulations in reanalysis wind fields (Fig. 12).

(ii) The total area covered by tracers grows *linearly* in the tank (Fig. 8), the behavior is similar in the numerical experiments for intermediate times (Fig. 13, inset). The long-time dynamics reflects diffusive slowdown in the atmosphere (Fig. 13), but this regime is not accessible in the laboratory setup.

(iii) The speed of dispersal (slope parameters and encompassing time) is determined by the thermal Rossby number Eq. (4) obeying empirical scaling relations Figs. 6, 7, and 9.

(iv) Important results of the numerical advection tests are that the mean pair separation strongly depends on the initial value r_0 and follows t^2 growth [Fig. 16(a)], similarly to the Batchelor hypothesis. A relevant consequence is that an extended tracer cloud exhibits always a mixed behavior, therefore a direct relationship between pair separation and overall statistics cannot be easily formulated.

(v) The slopes of mean pair separation do not follow the Batchelor scaling, the apparent exponent value is 5/3 [Fig. 16(b)]. In contrast to Eqs. (6) and (7), simple dimensional considerations suggest a combination like $U^{-3}(\epsilon r_0)^{5/3}$, where U has a dimension of velocity. However, the appearance of such a factor seems to be difficult to argue for. Further work is needed to explain these observations.

(vi) The quasigeostrophic turbulent wind field is far from being homogeneous and isotropic, large scale (irregular) eddies determine the dynamics. In addition, reanalysis fields do not resolve structures below the grid spacing. Consequently, the collective dynamics of an extended tracer cloud is

spoiled by pairs of initial separation below gridsize. An obvious sign of this effect is the appearance of unrealistically long initial transients at too small cloud sizes, where the "true" dynamics unfolds only when the mean pair separation definitely exceeds the size of cells. This observation might help to clarify earlier results on scaling behavior of tracers simulated in wind fields of limited resolutions [22,41].

ACKNOWLEDGMENTS

[1] *Hemispheric Transport of Air Pollution 2007*, Air Pollution Studies No. 16, edited by the Task Force on Hemispheric Transport of Air Pollution (United Nations Publication, New York, 2007).

[2] *Air Pollution Modelling and Simulation*, edited by B. Sportisse (Springer, Berlin, 2002).

[3] M. Z. Jacobson, *Air Pollution* (Cambridge University Press, Cambridge, England, 2002).

[4] A. Stohl, C. Forster, A. Frank, P. Seibert, and G. Wotawa, Atmos. Chem. Phys. **5**, 2461 (2005).

[5] *Transport and Mixing in Geophysical Flows*, edited by J. B. Weiss and A. Provenzale (Springer, Berlin, 2008).

[6] R. X. Huang, *Ocean Circulation: Wind-Driven and Thermohaline Processes* (Cambridge University Press, Cambridge, England, 2010).

[7] M. Ollitrault, C. Gabillet, and A. Colin de Verdiere, J. Fluid Mech. **533**, 381 (2005).

[8] I. Koszalka, J. H. LaCasce, and K. A. Orvik, J. Mar. Res. **67**, 411 (2009).

[9] P. Morel and W. Bandeen, Bull. Am. Meteorol. Soc. **54**, 298 (1973).

[10] P. Morel and M. Larcheveque, J. Atmos. Sci. **31**, 2189 (1974).

[11] P. Jullian, W. Massman, and N. Levanon, Bull. Am. Meteorol. Soc. **58**, 936 (1977).

[12] J. Er-El and R. Peskin, J. Atmos. Sci. **38**, 2264 (1981).

[13] R. B. Rood, Rev. Geophys. **25**, 71 (1987).

[14] A. Staniforth and J. Côté, Mon. Weather Rev. **119**, 2206 (1991).

[15] L. Illari, J. Marshall, P. Bannon, J. Botella, R. Clark, T. Haine, A. Kumar, S. Lee, K. J. Mackin, G. A. McKinley, M. Morgan, R. Najjar, T. Sikora, and A. Tandon, Bull. Am. Meteorol. Soc. **90**, 1619 (2009).

[16] J. P. L. C. Salazar and L. R. Collins, Annu. Rev. Fluid Mech. **41**, 405 (2009).

[17] M. Bourgoin, N. T. Ouellette, H. Xu, J. Berg, and E. Bodenschatz, Science **311**, 835 (2006).

[18] D. Fultz, J. Atmos. Sci. **6**, 17 (1949); **9**, 379 (1952).

[19] D. Fultz, R. R. Long, G. W. Owens, W. Bohan, R. Kaylor, and J. Weil, Meteorol. Monogr., Amer. Meteorol. Soc. **4**, 1 (1959).

[20] R. Hide, Q. J. R. Meteorol. Soc. **79**, 161 (1953); Philos. Trans. R. Soc. London, Ser. A **250**, 441 (1958).

[21] W. W. Fowlis and R. Hide, J. Atmos. Sci. **22**, 541 (1965).

[22] M. Huber, J. C. McWilliams, and M. Ghil, J. Atmos. Sci. **58**, 2377 (2001).

[23] A. C. Haza, A. C. Poje, T. M. Özgökmen, and P. Martin, Ocean

Model. **22**, 48 (2008).

[24] B. Gyüre, I. Bartos, and I. M. Jánosi, Phys. Rev. E **76**, 037301 (2007).

[25] R. Salmon, *Lectures on Geophysical Fluid Dynamics* (Oxford University Press, New York, 1998).

[26] R. Hide and P. J. Mason, Adv. Phys. **24**, 47 (1975).

[27] J. R. Holton, *An Introduction to Dynamic Meteorology*, 4th ed. (Academic Press, Burlington, 2004).

[28] R. T. Pierrehumbert and K. L. Swanson, Annu. Rev. Fluid Mech. **27**, 419 (1995).

[29] G. K. K. Vallis, *Atmospheric and Oceanic Fluid Dynamics* (Cambridge University Press, Cambridge, England, 2006).

[30] A. Stohl and P. Seibert, Q. J. R. Meteorol. Soc. **124**, 1465 (1998).

[31] A. Stohl, Atmos. Environ. **32**, 947 (1998).

[32] S. M. Uppala *et al.*, Q. J. R. Meteorol. Soc. **131**, 2961 (2005).

[33] http://www.ecmwf.int/research/era/do/get/era-interim

[34] P. Kiss, L. Varga, and I. M. Jánosi, J. Renewable Sustainable Energy **1**, 033105 (2009).

[35] J. M. Ottino, *The Kinematics of Mixing: Stretching, Chaos, and Transport* (Cambridge University Press, Cambridge, England, 1989).

[36] T. Tél and M. Gruiz, *Chaotic Dynamics: An Introduction Based on Classical Mechanics* (Cambridge University Press, Cambridge, England, 2006).

[37] R. D. Sardeshmukh and B. Liebmann, J. Climate **6**, 569 (1993).

[38] M. R. Schoeberl, A. R. Douglass, Z. Zhu, and S. Pawson, J. Geophys. Res. **108**, 4113 (2003).

[39] A. Stohl, G. Wotawa, P. Seibert, and H. Kromp-Kolb, J. Appl. Meteorol. **34**, 2149 (1995).

[40] W. H. Press, A. A. Teukolsky, W. T. Vetterling, and B. P. Flannery, *Numerical Recipes in C: The Art of Scientific Computing*, 2nd ed. (Cambridge University Press, Cambridge, England, 1992).

[41] R. T. Pierrehumbert and H. Yang, J. Atmos. Sci. **50**, 2462 (1993).

[42] S. B. Pope, *Turbulent Flows* (Cambridge University Press, Cambridge, England, 2000).

[43] N. T. Ouellette, H. Xu, M. Bourgoin, and E. Bodenschatz, New J. Phys. **8**, 109 (2006).

[44] G. K. Batchelor, Q. J. R. Meteorol. Soc. **76**, 133 (1950).

[45] P. Tabeling, Phys. Rep. **362**, 1 (2002).

[46] E. P. Gerber and G. K. Vallis, J. Atmos. Sci. **64**, 3296 (2007).

[47] D. K. Lilly, J. Atmos. Sci. **40**, 749 (1983).